ACTA IMEKO
ISSN: 2221-870X
June 2026, Volume 15, Number 2, 1 – 10

Characterization of high-reflectance diffuse coatings for 3D-printed optics

Giovanni Gibertoni[1,2], Luigi Rovati[1]

[1] *Department of Engineering "Enzo Ferrari", University of Modena and Reggio Emilia, Italy*
[2] *Department of Biomedical, Metabolic and Neural Sciences, University of Modena and Reggio Emilia, Italy*

ABSTRACT
Low-cost diffuse reflectance coatings were characterized for use on 3D-printed optical assemblies. Barium sulfate ($BaSO_4$) and titanium dioxide (TiO_2) suspensions were deposited on polylactic acid (PLA) substrates through a multilayer drop-casting process with an acrylic binder, and compared to commercial white paints and Spectralon® standards. Hemispherical reflectance was measured using an integrating sphere over the 300 nm to 1000 nm range, while angular scattering was assessed from −85° to 85° using a collimated xenon source. $BaSO_4$ achieved the highest broadband performance, with a mean hemispherical reflectance of 98.9 % and a mean angular deviation of 6.3 % from the ideal cosine law. TiO_2 showed slightly lower reflectance (96.6 %) and stronger angular directionality, consistent with its smoother and glossier surface finish. Commercial acrylic coatings exhibited markedly lower reflectance (70 % to 86 %) and large deviations from cosine behaviour, while office paper provided good diffusivity but insufficient spectral uniformity. The results demonstrate that a simple $BaSO_4$-based coating can deliver stable, broadband, and highly diffuse reflectance when applied to 3D-printed substrates, enabling the fabrication of low-cost optical diffusers and reflectance references for custom laboratory setups.

Section: RESEARCH PAPER

Keywords: diffuse reflectance; high-reflectance coatings; Lambertian behaviour; 3D-printed optics; BRDF

Citation: G. Gibertoni, L. Rovati, Characterization of high-reflectance diffuse coatings for 3D-printed optics, Acta IMEKO, vol. 15 (2026) no. 2, pp. 1–10. DOI: 10.21014/actaimeko.v15i2.2253

Section Editor: Maik Rosenberger, Ilmenau University of Technology, Germany

Received: November 28, 2025; **In Final Form:** April 17, 2026; **Published:** June, 2026.

Funding: No funding specified.

Corresponding Author: Giovanni Gibertoni, e-mail: giovanni.gibertoni@unimore.it

1. INTRODUCTION

Highly reflective coatings play a fundamental role across optical, photonic, and measurement sciences. They ensure efficient light collection, controlled radiative transfer, and reproducible reference conditions in metrological and experimental setups.

Applications range from spectrophotometry and radiometry to laser diagnostics, solar control, and biomedical optics [1], [2]. The performance of these coatings depends on both their spectral reflectance and angular scattering properties, which determine whether they behave as specular mirrors, diffuse reflectors, or intermediate surfaces.

Among diffuse reflectors, *Lambertian* materials are particularly valuable because they exhibit constant radiance regardless of viewing direction, providing uniform luminance for calibration and illumination purposes [3]. Such materials are indispensable in photometric and radiometric systems, including integrating spheres, reflectance standards, and diffuse illumination cavities [4]–[6]. Historically, a variety of formulations have been explored: magnesium oxide, polytetrafluoroethylene (PTFE), and barium sulfate ($BaSO_4$) have become the most widespread choices due to their stability and broadband reflectance [2], [7], [8]. Commercial coatings such as Spectralon®, Avian-B, and Labsphere 6080 are now established references for high-diffusivity surfaces [9]–[11]. Parallel research has also investigated TiO_2 and composite pigments with enhanced scattering and near-infrared reflectance [12]–[14], extending the applicability of these materials to both optical and energy-management systems.

In the field of optics and photonics, diffusely reflective coatings play a key role in applications requiring controlled or homogeneous illumination, such as metrological systems, calibration setups, and optical instruments based on uniform light distribution. Integrating spheres, light-mixing cavities, and Ganzfeld stimulators rely on such coatings to generate uniform radiance fields [15]–[17]. Uniform diffuse illumination is also crucial in a number of ophthalmic and vision-science instruments—such as full-field electroretinography, pupillometry, visual-field stimulators, and other testing devices—where luminance homogeneity directly affects the reliability of the recorded responses [18], [19].

In parallel with the evolution of reflective materials, laboratory optics has progressively adopted modular, customizable architectures, as modern experimental setups frequently demand tailor-made elements, such as optical mounts, enclosures, baffles, or diffusive cavities, which cannot be sourced from standard catalogues. Additive manufacturing offers a flexible, cost-effective approach for rapid prototyping of lightweight optical components with tailored geometries [20]–[24]. 3D printing has been used to fabricate mechanical supports, optical enclosures, functional photonic components, and even printed optics, such as lenses, light guides, mirrors, and complex illumination elements made directly from polymeric materials [20]–[27]. However, despite this progress, few studies have explored diffusely reflective coatings on 3D-printed substrates. Printable polymers such as PLA and and acrylonitrile butadiene styrene (ABS) possess inherently low reflectance and poor surface uniformity, which makes them unsuitable for applications requiring diffuse scattering or Lambertian behaviour; achieving adequate optical performance therefore requires coating the printed parts with a high-reflectance, diffusively scattering layer that enhances broadband reflectance while preserving a uniform matte finish.

Within this framework, building on our preliminary work [28], the present study investigates the spectral and angular performance of two diffusely reflective coatings, $BaSO_4$ and TiO_2, manually applied to 3D-printed substrates using a multilayer drop-casting procedure. The goal is to assess their suitability for constructing compact and affordable optical components, such as diffusive reflectors, integrating spheres, and custom laboratory assemblies. To contextualize their performance, the coatings are compared with calibrated commercial references (Spectralon® standards) and with readily available white surfaces, including a matte acrylic spray paint, a brush-applied titanium white acrylic paint, and standard office paper. Commercial diffuse standards offer excellent performance but are expensive and not always practical for repeated or large-area use; in contrast, the simple coatings examined here aim to provide a reproducible and low-cost alternative for optical calibration tasks and experimental prototyping.

2. THEORETICAL BACKGROUND AND RELATED WORKS

2.1. Principles of diffuse reflectance

The reflectance components of a surface express the ratio between the reflected and incident radiant flux, and their angular dependence determines whether the material behaves as a specular, diffuse, or mixed reflector [3], [4]. For an ideally diffuse or *Lambertian* surface, the reflected radiance L_r is constant with respect to the viewing direction, as the surface reflects light uniformly into the hemisphere. According to Lambert's cosine law, the radiant intensity $I_r(\theta_r)$ follows:

$$I_r(\theta_r) \propto \cos\theta_r. \tag{1}$$

Consequently, the reflected radiance is defined as:

$$L_r = \frac{\rho\, E_i}{\pi}, \tag{2}$$

where ρ is the surface reflectance (or albedo) and E_i the incident irradiance. The corresponding bidirectional reflectance distribution function (BRDF) is theoretically constant:

$$f_r(\theta_i, \theta_r, \phi_r - \phi_i) = \frac{\rho}{\pi}. \tag{3}$$

This implies that while the radiant flux per unit solid angle decreases with $\cos\theta_r$, the apparent surface area decreases by the same factor, resulting in uniform luminance regardless of the viewing angle [3]. Lambertian behavior is essential in optical metrology and calibration tasks to ensure predictable light distribution.

Diffuse reflectance can be characterized through two complementary approaches. Hemispherical methods, such as measurements performed with integrating spheres, provide the total reflected flux integrated over the entire observation hemisphere [5], [29]. Angularly resolved setups measure the bidirectional reflectance factor or distribution function, and describe how the reflected intensity varies with viewing direction. Real coatings only approximate the Lambertian ideal, since microstructure, grain size, binder transparency, and film thickness influence both the total reflectance and the angular behaviour. Accurate metrological characterisation is therefore required whenever low-cost or custom coatings are introduced into optical systems.

2.2. Commercial high-reflectance coatings

Several commercial materials provide stable and well-characterized diffuse reflection, serving as a benchmark for optical and photometric measurements. Table 1 summarizes the most widely used coatings and reference standards. Spectralon® [9], [30] is a sintered PTFE material with reflectance above 98 % across the 250 nm to 2500 nm range and nearly perfect Lambertian behavior. Water-based $BaSO_4$ coatings, such as Labsphere 6080 and Avian-B offer similar VIS reflectance at a lower cost [10], [11], while inorganic formulations like Gigahertz ODP97 improve durability for repeated use [31]. Other PTFE films (e.g., GORE Diffuse Reflector) provide flexible high-reflectance liners for optical housings [2]. Other studies, such as Janeček [2], compared a wide range of commercial reflectors—including PTFE, $BaSO_4$, TiO_2 paints, and MgO—confirming that PTFE-based materials maintain reflectance above 0.95 in the 380 nm to 500 nm range, whereas TiO_2 coatings show steeper spectral drop-off below 420 nm.

Table 1. Characteristics of commercial high-reflectance coatings and reference materials.

Coating / material	Base composition	Reflectance (VIS)	Ref.
Labsphere 6080	$BaSO_4$	≈ 98 %	[11]
Avian-B / Avian-D	$BaSO_4$ (acrylic)	97 % to 98 %	[10]
Gigahertz ODP97	$BaSO_4$ (inorganic binder)	≈ 97 %	[31]
Spectralon®	PTFE (sintered)	98 % to 99 %	[9], [30]
GORE Diffuse Reflector	PTFE film	> 95 %	[2]
Ti-Pure R-706 / Tiona	TiO_2	90 % to 96 %	[13], [32]
MgO coatings	MgO powder (inorganic)	> 95 %	[7]

2.3. Laboratory and low-cost coatings

Despite their excellent optical performance, commercial coatings can be expensive, difficult to reapply, or incompatible with custom geometries, such as 3D-printed optical parts. For this reason, low-cost or in-house formulations have become increasingly relevant in laboratory environments, where ease of preparation and material availability are critical.

A first distinction concerns the cost and availability of raw inorganic powders. Prices vary substantially across suppliers and material grades: $BaSO_4$ ReagentPlus® (99 % purity) is listed at approximately 287 €/kg for 1 kg lots at Sigma-Aldrich, whereas TiO_2 rutile (99.9 % purity or higher, particle size below 5 μm) can reach 800 €/kg in comparable quantities. These reagent-grade materials command higher prices due to controlled particle-size distributions, certified purity, and batch documentation. Conversely, non-specialized e-commerce suppliers offer pigment-grade powders

at a considerably lower cost—typically 15 €/kg to 20 €/kg for $BaSO_4$ and 18 €/kg to 30 €/kg for TiO_2—albeit without formal certificates of analysis. In the context of this investigation, however, the optical behaviour of such low-cost grades proved largely comparable to that of their higher-purity counterparts when formulated into diffuse reflective coatings.

Within this framework, several coating strategies have been explored in the literature. A $BaSO_4$-based spray coating applied on metal and polymer substrates was reported to achieve an average reflectance of 94.9 % between 400 nm and 1600 nm, with close-to-Lambertian characteristics [8]. $BaSO_4$ nanoparticle paints were shown to exhibit solar reflectance up to 98 % and strong mid-infrared emissivity [14], while TiO_2 nanoparticle films were reported to achieve reflectance values around 0.9 in the visible range [13].

These results align with the intrinsic physical properties of $BaSO_4$ and TiO_2, which remain the most effective pigments for diffusive white surfaces. Both are chemically stable inorganic oxides with high refractive indices—approximately 1.64 for $BaSO_4$ and 2.7 for TiO_2—and their scattering behaviour is strongly influenced by particle size distribution. Finer TiO_2 particles typically yield denser, glossier films, whereas the coarser morphology of $BaSO_4$ favours matte, highly diffusive coatings.

Balancing cost, accessibility, and optical performance, these materials enable the fabrication of custom, highly reflective diffusers suitable for nonstandard or custom geometries. When properly formulated and applied, they provide a practical alternative to commercial white standards. This makes them especially attractive for laboratories developing bespoke optical components or prototypes, which motivates the application strategies and practical guidelines discussed in the following section.

3. MATERIALS AND METHODS

This section describes the materials selected for diffuse reflectance testing and the experimental procedures used to evaluate their optical behavior. Five representative coatings were prepared: two powder-based $BaSO_4/TiO_2$ formulations and three commercial or readily available white surfaces, covering both laboratory-grade and low-cost alternatives. Their performance was assessed through hemispherical spectral reflectance measurements and angular scattering analysis using a custom BRF setup. The following subsections detail sample preparation, coating procedures, and the characterization systems.

3.1. Samples tested

All reflective samples under test were fabricated on 3D-printed PLA substrates (30 mm×30 mm flat plates). The surfaces were manually sanded up to grit 600 to remove layer artifacts and improve coating adhesion. Five materials have been evaluated:

1) $BaSO_4$ powder coating with acrylic binder;
2) TiO_2 powder coating with acrylic binder;
3) Acrylic spray paint (Pure White Matt, RAL 9010);
4) Brush-applied acrylic paint (Titanium White 105);
5) Standard white paper (80 g/m^2).

3.1.1. Powder-based coatings

Several coating techniques are commonly employed to obtain diffusely reflective surfaces, depending on the required uniformity and substrate geometry [8], [13], [14]. Among them, *dip coating*, *drop casting with spin coating*, and *spray coating* are the most widely adopted for laboratory-scale fabrication of optical coatings, as illustrated in Figure 1.

In dip coating, the substrate is immersed in a suspension and withdrawn at a controlled rate, producing a uniform film through

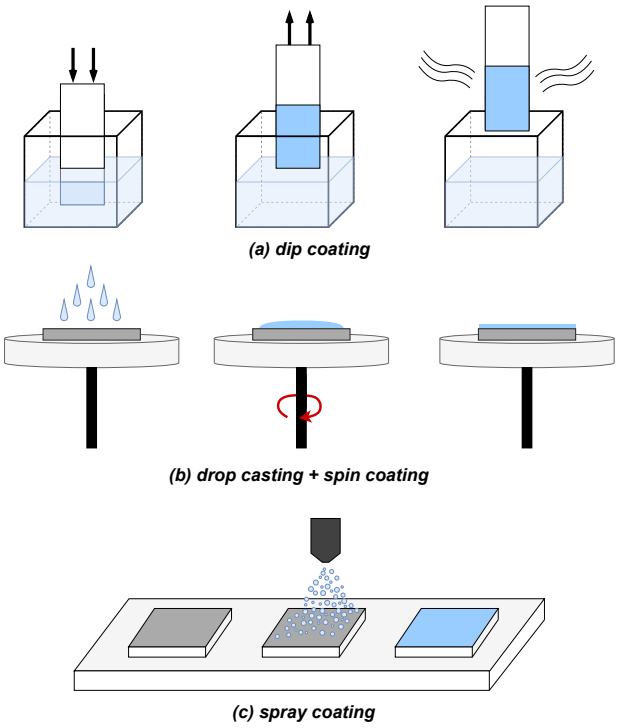

Figure 1. Schematic representation of three coating techniques: (a) dip coating, (b) drop casting + spin coating, and (c) spray coating.

gravitational drainage and solvent evaporation. Drop casting and spin coating rely on the spreading of small liquid droplets on a static or rotating substrate, where film thickness is governed by the droplet volume, viscosity, and surface tension, yielding smooth dried layers once the solvent evaporates. Spray coating atomizes the suspension through a pressurized nozzle, enabling thin and homogeneous deposition over flat or curved surfaces, with fine control of layer thickness and particle dispersion [8], [12], [14].

For powder-based coatings, $BaSO_4$ powder (99.5 % purity, D_{50} = 0.7 μm) and TiO_2 powder (98 % purity, rutile phase, $D_{50} \approx$ 200 nm to 300 nm) were obtained from CARLO ERBA Reagents srl (Via Raffaele Merendi 22, 20007 Cornaredo, MI, Italy). During the experimental evaluation, particle size was identified as a key parameter governing both suspension rheology and the resulting coating morphology. Finer TiO_2 dispersions exhibited higher viscosities and produced more compact, continuous films characterized by increased surface gloss, whereas coarser $BaSO_4$ particles promoted enhanced diffuse light scattering, leading to a more pronounced matte appearance.

The powders were dispersed in distilled water at 30 % w/w and magnetically stirred for 10 min to ensure a homogeneous suspension. Proper mixing is essential because sedimentation or particle agglomeration adversely affects film uniformity and optical performance. Each coated sample was fabricated through five sequential layers, applying the following procedure for each:

- a uniform drop-cast layer was deposited by dispensing a measured volume of suspension using a 3 mL disposable plastic pipette and allowing it to spread evenly. For larger or curved substrates, gentle high-frequency tapping or slow rotational motion was used to promote uniform coverage and reduce thickness gradients;
- the layer was allowed to dry completely; water-based suspensions typically required longer drying times compared to alcohol-based solutions (e.g., IPA or ethanol);

- light sanding of the dried layer was performed using grit 1000 abrasive paper to remove microscopical irregularities, reduce gloss, and improve the surface's overall homogeneity for subsequent layers;
- a very thin coating of transparent acrylic binder (Dupli-Color Firnis Spray Acrylic, Transparent Matte, product code 319747) was applied to protect the deposited pigment, limit particle detachment, and enhance inter-layer adhesion.

After the final drying step, the coated surfaces were lightly polished to obtain a uniform matte finish with minimal specular contribution.

3.1.2. Commercial paints

In addition to the powder-based coatings, two commercial white paints and a reference paper surface were evaluated for comparison. The first coating was a RAL acrylic spray paint (Dupli-Color RAL Acryl, Pure White Matte, RAL 9010; product code 349805), manufactured by European Aerosols GmbH (Iserlohn, Germany). According to the technical data sheet, this paint exhibits a matte gloss level of 10 ± 2 GU at 60° (DIN 67530) [33]. The paint was applied according to the manufacturer's instructions, and a total of six thin layers were deposited over the PLA substrate.

The second commercial material was a brush-applied acrylic paint (Amsterdam Standard Series, Titanium White 105), manufactured by Royal Talens B.V. (Apeldoorn, Netherlands), a water-based TiO_2-pigmented formulation intended for fine-arts applications [34]. Four homogeneous layers were applied to the PLA substrate and allowed to dry completely before measurement. Finally, light sanding with grit 600 was performed to homogenize the surface, removing brush marks and reducing residual non-uniformities.

As a final sample, a standard white office paper was included for comparison (Navigator™ Universal Office White Paper, 80 g/m^2, Art. No. 006102), manufactured by The Navigator Company S.A. (Lisbon, Portugal), representing a commonly available diffuse white surface. Four stacked sheets were used and attached to the PLA support by folding the edges and taping them on the back of the substrate, ensuring that the original surface of the paper remained unaltered.

Table 2 summarizes all samples and their key properties.

Table 2. Summary of tested coatings, acronyms, color identifiers, application methods, and key properties.

Coating	Acronym	Color	Application	Key properties
$BaSO_4$ powder	**BaSO4**	•	Drop casting; sanding; acrylic binder	Highly diffusive; matte; stable
TiO_2 powder	**TiO2**	•	Drop casting; sanding; acrylic binder	Bright; less diffusive; crack-prone
Matte acrylic spray paint	**ASP**	•	Spray coating	Matte acrylic; 10 ± 2 GU at 60°
Acrylic titanium white	**ATW**	•	Brush applied; sanding	Water-based TiO_2 paint
Office white paper (80 g/m^2)	**OWP**	•	None	Smooth cellulose; bright white

3.2. Optical characterization setups

Two complementary configurations were used to evaluate the optical performance of the coatings:

A. **Hemispherical spectral reflectance** for broadband reflectance characterization;

B. **Bidirectional reflectance factor (BRF)** for angular scattering analysis.

A. Hemispherical spectral reflectance

Total hemispherical reflectance was measured using an integrating sphere (ARC-LIGHT-50HAL, Arcoptix SA, Neuchâtel, Switzerland) illuminated by a 12 W halogen lamp and coupled to a compact spectrometer (Qmini, Broadcom Inc., San José, CA, USA) operating over the 200 nm to 1000 nm range (see Figure 2). This configuration allowed for the simultaneous collection of diffuse and specular components without requiring external alignment. All coatings listed in Table 2, along with the four calibrated Spectralon® standards (REF 02, REF 50, REF 75, and REF 99; Labsphere Inc., North Sutton, NH, USA), were characterized under identical conditions following thermal stabilization of the source.

To rigorously assess spectral consistency and robustness, a total of $N = 12$ measurements were acquired for each sample across six independent sessions (indexed as $k = 1, \ldots, 6$) performed on different days. Each session comprised two acquisitions with sample repositioning to evaluate short-term repeatability, while different optical fibers were employed across sessions to incorporate the variability introduced by practical setup reconfigurations. This protocol provided a comprehensive characterization of the broadband spectral behavior and stability of the tested coatings (see Figure 2).

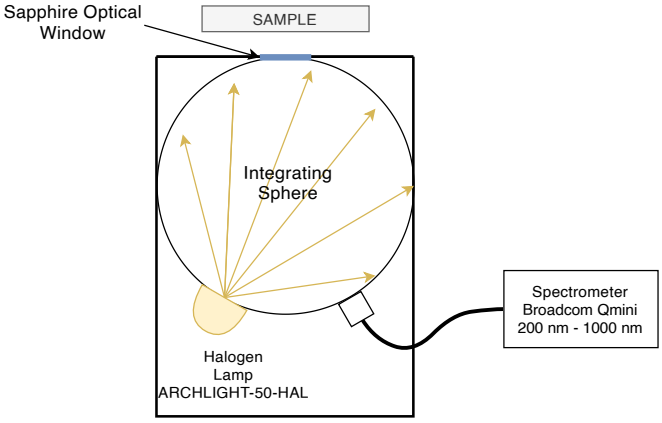

Figure 2. Spectral measurement system for hemispherical reflectance characterization. The integrating sphere (ARC-LIGHT-50HAL) is illuminated by a 12 W halogen lamp and coupled to a Qmini spectrometer (Broadcom Inc., USA). Four calibrated Spectralon® standards (2 % to 99 %) were used as reflectance references.

B. Bidirectional reflectance factor setup

The bidirectional reflectance factor (BRF) was evaluated using a collimated 150 W xenon arc lamp (SLS401, Thorlabs Inc., Newton, NJ, USA) positioned at $d_{src} = 500$ mm from the sample (see Figure 3). With a characteristic beam divergence of $\alpha_{div} = 3.2°$ (half-angle), the source produced a spot diameter of approximately $D_b \approx 91$ mm at the sample plane under normal incidence, ensuring full illumination of the target area. Reflected radiant power was collected by a calibrated optical power meter (Model 1918-R with 918D-UV-OD3R Si detector, Newport Corporation, Irvine, CA, USA) mounted on a rotation stage (OCT-XYR1/M, Thorlabs Inc.) to enable angular scanning between −85° and 85°. The detector was placed at $d_{det} = 390$ mm and coupled to a 63.5 mm long cylindrical viewing tube with a $D_{ap} = 5$ mm aperture. This geometry defined the system's geometric collection parameters, where α_{acc} denotes the acceptance half-angle, α_{FOV} the angular

field of view, and D_{spot} the diameter of the detection area on the sample surface:

$$\begin{cases} \alpha_{acc} = 0.73° \\ \alpha_{FOV} = 9° \\ D_{spot} \approx 56\,\text{mm} \end{cases} \tag{4}$$

Measurements were performed on the complete set of samples listed in Table 2. Each specimen was mounted individually, ensuring precise alignment of its front surface with the rotation axis of the stage to minimize geometric errors during scanning. To provide a reliable benchmark, the same 99 % Spectralon® standard (Labsphere Inc.) used in the hemispherical characterization was also measured under identical conditions.

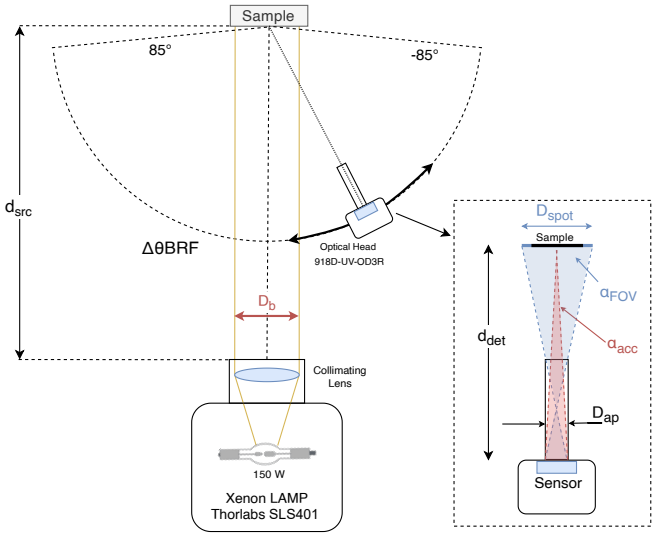

Figure 3. Angular reflectance measurement setup. A collimated xenon lamp (SLS401, Thorlabs Inc.) illuminates the sample at normal incidence. The reflected power is collected by a 1918-R power meter equipped with a 918D-UV-OD3R detector and a 63.5 mm tube (D_{ap} = 5 mm), defining an acceptance angle of α_{acc} = 0.73° and a field of view of α_{FOV} = 9°. The detector scans between −85° and 85° around the sample center.

The measured angular reflectance profile $R(\theta)$ was normalized by its maximum value R_{max} over the angular range $\Theta = [-85°, 85°]$, yielding

$$R_{norm}(\theta) = \frac{R(\theta)}{R_{max}} \cdot 100\,\%. \tag{5}$$

The ideal reference profile corresponds to Lambertian diffusion, $R_{ideal}(\theta) \propto \cos\theta$, scaled so that $R_{ideal}(0°) = 100\,\%$.

The metrics in Table 5 were computed over the discrete angle set Θ. The mean relative error $\Delta\bar{R}$ and maximum relative error ΔR_{max} quantify the deviation from $R_{ideal}(\theta)$ and are expressed in percent.

The bilateral symmetry index Σ measures left–right agreement:

$$\Sigma = \frac{1}{|\Theta^+|} \sum_{\theta \in \Theta^+} \left| R_{norm}(+\theta) - R_{norm}(-\theta) \right|, \tag{6}$$

where $\Theta^+ = \{\theta > 0 \mid \theta \in \Theta\}$.

The normalized directionality coefficient Q_{Corr} quantifies how closely the measured profile follows the Lambertian angular shape:

$$Q_{Corr} = \frac{Q_{Meas}}{Q_{Ideal}} = \frac{R_{norm}(0°)/\bar{R}_{norm}}{R_{ideal}(0°)/\bar{R}_{ideal}}, \tag{7}$$

where $\bar{R}_{norm}$ and $\bar{R}_{ideal}$ are the mean values of the corresponding profiles over the valid angle set.

A perfectly Lambertian surface yields $Q_{Corr} = 1.0$. Values $Q_{Corr} > 1$ indicate a more directional (super-Lambertian) profile, where reflectance is relatively higher near normal incidence. Conversely, $Q_{Corr} < 1$ denotes a flatter, more diffuse (sub-Lambertian) angular distribution.

3.3. Calibration of hemispherical reflectance data

All measurements acquired with the hemispherical setup described in Section 3.2. were processed using a dedicated three-step calibration procedure designed to compensate for changes in dark offset, optical fiber coupling, illumination intensity, and small non-linearities in the integrating sphere response.

3.3.1. Session-specific normalization

For each independent measurement session k (with $k = 1, \ldots, 6$), characterized by a specific state of optical fiber coupling and source stability, the spectra acquired from the 2 % and 99 % Spectralon standards were averaged to generate two session-specific reference curves, $S_{02,k}(\lambda)$ and $S_{99,k}(\lambda)$. These curves define the effective dynamic range for that specific session. Consequently, every raw spectrum $S^{(k)}(\lambda)$ acquired during session k was mapped onto a normalized reflectance scale via:

$$r^{(k)}_{scaled}(\lambda) = 2 + \frac{S^{(k)}(\lambda) - S_{02,k}(\lambda)}{S_{99,k}(\lambda) - S_{02,k}(\lambda)} \cdot (99 - 2), \tag{8}$$

which enforces the boundary conditions for every wavelength λ:

$$r^{(k)}_{scaled}(\lambda) = 2\,\% \quad \text{if} \quad S^{(k)}(\lambda) = S_{02,k}(\lambda),$$

$$r^{(k)}_{scaled}(\lambda) = 99\,\% \quad \text{if} \quad S^{(k)}(\lambda) = S_{99,k}(\lambda).$$

This local normalization compensates for session-dependent variations in detector offset, fiber throughput, and lamp intensity, whilst preserving the spectral features of the measurement.

3.3.2. Construction of a global calibration curve

Following the session-specific normalization, the scaled reflectance values corresponding to all nominal standards (2 %, 50 %, 75 %, and 99 %) were aggregated from all sessions to compute four global calibration nodes (x_i, R_i). Since the system response exhibited slight non-linearities, these points deviated from the ideal identity line. A monotone cubic Hermite interpolating polynomial (PCHIP) was fitted to these nodes, yielding a smooth, strictly increasing global calibration function $R = f(r_{scaled})$.

3.3.3. Application of the calibration function

The global calibration function was finally applied to every normalized spectrum to obtain the accurate reflectance:

$$R_{calibrated}(\lambda) = f\left(r^{(k)}_{scaled}(\lambda)\right). \tag{9}$$

This step produces linearized reflectance curves (in percent units), effectively correcting for the intrinsic non-linearity of the hemispherical measurement system while maintaining the robustness of the session-based drift compensation.

4. RESULTS

4.1. Validation of the calibration method

To validate the three-step calibration workflow detailed in Section 3.3., the spectral consistency of the four reference standards (REF02, REF50, REF75, REF99) has been analyzed. A total of $N = 12$ individual measurements were acquired across six independent sessions (indexed as $k = 1, \ldots, 6$), performed on varying days and with different fiber-coupling configurations.

This validation step is critical to ensure that the combination of session-specific normalization (via $S_{02,k}$ and $S_{99,k}$) and global correction effectively mitigates the systematic errors and non-linearities introduced by the experimental setup.

Figure 4 demonstrates the effectiveness of the global PCHIP correction. To strictly evaluate linearity, the plot displays the normalized response ratio $\rho_{\text{norm}} = R_{\text{meas}}/R_{\text{nom}}$ against the nominal targets. Unlike the raw system response, the calibrated data exhibit near-perfect behavior, with the experimental points tightly clustered around the ideal unity line ($\rho_{\text{norm}} = 1.0$). This confirms that the non-linearities identified in the raw signals have been successfully compensated, leaving only negligible residuals across the dynamic range.

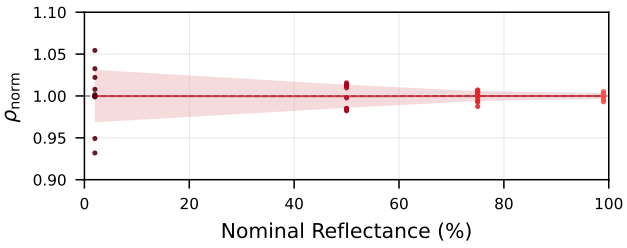

Figure 4. Linearity verification of the calibrated system. The plot shows the normalized response $\rho_{\text{norm}} = R_{\text{meas}}/R_{\text{nom}}$ for the four reference standards. The dashed line at $\rho_{\text{norm}} = 1.0$ indicates ideal linear behavior. Shaded areas represent standard deviation ($N = 12$).

The spectral performance of the calibration is detailed in Figure 5, which displays the profiles of the four standards across the 300 nm to 1000 nm bandwidth. The system demonstrates excellent spectral flatness and strong agreement with the nominal values (dashed lines) throughout the visible and near-infrared regions. This result highlights that, although the non-linearity correction applied is wavelength-independent (scalar), the spectral stability of the measurements is preserved, without introducing λ-dependent distortions across the analyzed range.

However, a notable increase in variability is observed in the 300 nm to 400 nm range, represented by the widening of the shaded standard deviation areas. This behavior is intrinsic to the tungsten-halogen light source used in the setup, which emits significantly lower irradiance in the near-UV/blue region compared to longer wavelengths, resulting in a reduced signal-to-noise ratio (SNR) in this specific band.

Table 3 provides a quantitative summary of the calibration performance. The post-correction accuracy is high, with the mean measured values deviating from the nominal targets by less than 0.03 %. Furthermore, the standard deviations remain consistently low (below 0.8 %) across all reference levels, confirming the high repeatability of the proposed method.

Table 3. Statistical performance of the calibration procedure ($N = 12$ independent measurements per reference). $\bar{R}_{\text{meas}}$ represents the spectrally averaged reflectance. Min_λ and Max_λ indicate the range of the *smoothed* spectral profile (assessing spectral flatness), while Std Dev quantifies the run-to-run repeatability.

Reference	R_{nom} (%)	$\bar{R}_{\text{meas}}$ (%)	Min_λ (%)	Max_λ (%)	Std Dev (%)	N
REF99	99.0	98.99	97.80	99.12	0.35	12
REF75	75.0	74.99	73.74	76.53	0.44	12
REF50	50.0	49.98	45.17	51.68	0.69	12
REF02	2.0	2.00	1.99	2.00	0.06	12

4.2. Spectral hemispherical reflectance

The calibrated reflectance spectra of all coatings were obtained using the validated three-step calibration procedure detailed in Section 3.3.. This method utilizes a four-point normalization based on certified Spectralon® standards [9] (REF02, REF50, REF75, REF99; Labsphere Inc., North Sutton, NH, USA). The initial local normalization maps the raw signal onto a scaled reflectance $r_{\text{scaled}}(\lambda)$, while the global PCHIP function corrects for the system's intrinsic non-linearities. The calibrated spectra were then smoothed using a Savitzky–Golay filter to reduce high-frequency noise. After calibration and smoothing, all spectra were merged across sessions, resampled onto a common wavelength grid (300 nm to 1000 nm), and averaged by coating type.

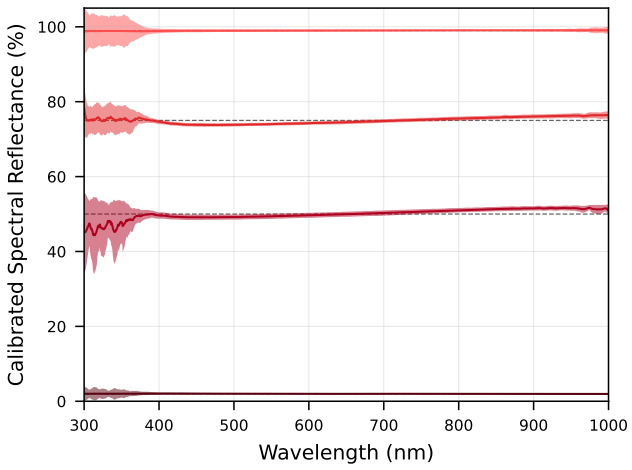

Figure 5. Calibrated spectral reflectance of the four reference standards (REF02, REF50, REF75, REF99) in the 300 nm to 1000 nm range. Solid lines depict the mean of $N = 12$ independent measurements; shaded regions indicate the standard deviation. The increased noise observed in the 300 nm to 400 nm range is due to the low spectral irradiance of the halogen source in the near-UV region.

Figure 6 presents the averaged hemispherical reflectance spectra obtained. In total, $N = 12$ independent measurements were analysed for each coating type, as summarized in Table 4.

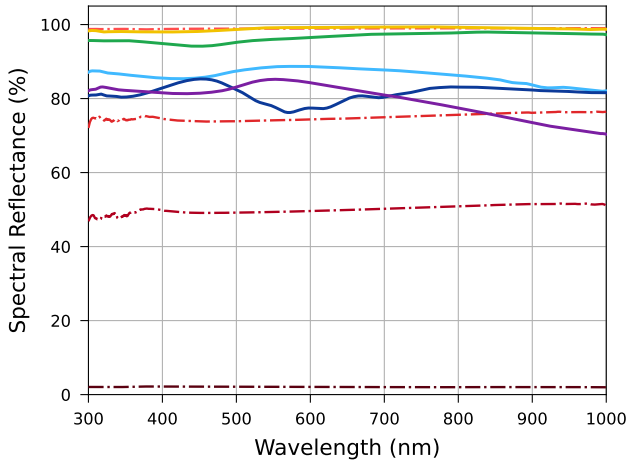

Figure 6. Spectral hemispherical reflectance of the tested coatings. Solid lines represent the mean reflectance for $BaSO_4$ (), TiO_2 (), ASP (), ATW (), and OWP (); dash-dotted lines correspond to the Spectralon® reference standards (REF02–REF99).

$BaSO_4$ exhibited the highest mean hemispherical reflectance over the full 300 nm to 1000 nm interval, with an average of 98.9 % and a very narrow dynamic range (from 98.0 % to 99.4 %). This behaviour closely matches the REF99 reference and confirms the excellent broadband uniformity of the coating. TiO_2 followed with a mean reflectance of 96.6 %, ranging

between 94.1 % and 98.0 %, showing a slightly larger spectral modulation but still retaining high overall reflectance.

Among the commercial coatings, the brush-applied acrylic white paint (ATW) reached a mean reflectance of 86.3 %, with values spanning from 81.9 % to 88.7 %. Acrylic spray paint (ASP) showed the widest variation, with an average of 79.7 % and a broad spectral range extending from 70.4 % to 85.2 %, reflecting its lower coating uniformity and stronger wavelength-dependent response. Office white paper (OWP) exhibited a mean reflectance of 81.4 %, but with a noticeable spread across the spectrum (from 76.2 % to 85.3 %), likely due to the combined effects of surface texture, coating finish, and optical brighteners.

Table 4. Hemispherical reflectance statistics over the 300 nm to 1000 nm spectral range.

Sample	AVG (%)	Min (%)	Max (%)	Std dev (%)	N
$BaSO_4$	98.9	98.0	99.4	0.49	12
TiO_2	96.6	94.1	98.0	1.22	12
ASP	79.7	70.4	85.2	4.29	12
ATW	86.3	81.9	88.7	1.89	12
OWP	81.4	76.2	85.3	2.15	12

Repeatability tests for $BaSO_4$ and TiO_2 coatings (Figure 7) confirmed the robustness of both the coating process and the multi-reference calibration. Independent measurements performed on different days with identical settings showed standard deviations below 1 % across the visible spectrum, indicating excellent repeatability of the hemispherical reflectance characterization.

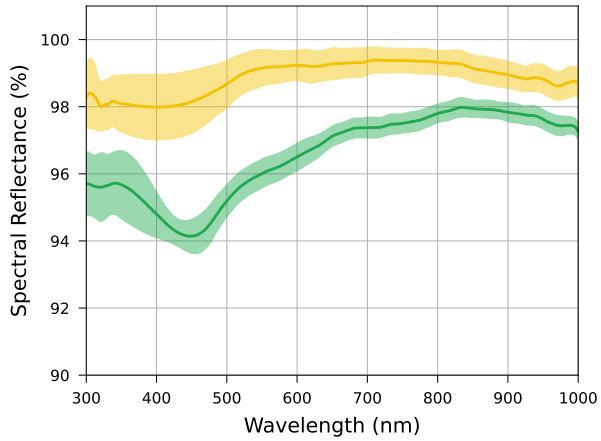

Figure 7. Repeatability of $BaSO_4$ (▬) and TiO_2 (▬) coatings measured on different days. Solid lines represent mean hemispherical reflectance; shaded areas indicate ± 1 across repeated measurements. The variation remained below 1 % across the visible range, confirming the stability of both the coating and the four-anchor calibration procedure.

4.3. Angular reflectance behavior

The angular dependence of diffuse reflectance was evaluated using the xenon-based measurement setup described in Section 3.2.. For each material, the reflected power was recorded between $-85°$ and $85°$ and converted into the normalized reflectance profile $R_{\text{norm}}(\theta) = 100 \cdot R(\theta)/R_{\text{max}}$, where R_{max} is the maximum value measured over the angular range (see Table 5 for the exact $R_{\text{norm}}(0°)$ values). The resulting profiles are shown in Figure 8, together with the ideal Lambertian response $R_{\text{ideal}}(\theta) \propto \cos\theta$ (dashed line).

All curves exhibit symmetry with respect to the optical axis and generally follow the expected cosine trend, with minor deviations at large viewing angles due to surface texture and residual specular components. Quantitative results are summarized in Table 5,

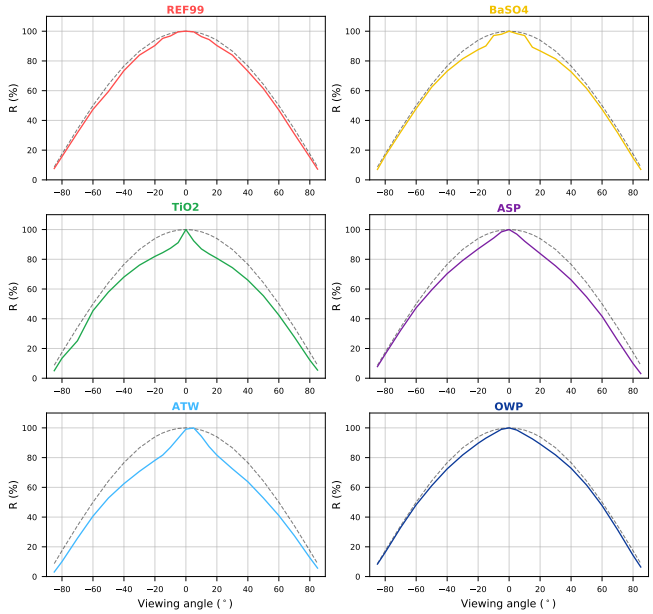

Figure 8. Angular reflectance profiles of all tested coatings and reference materials. Dashed black lines represent the ideal $R_{\text{ideal}}(\theta) \propto \cos\theta$ dependence of a Lambertian reflector.

reporting for each material the mean and maximum deviation from $R_{\text{ideal}}(\theta)$, the bilateral symmetry index Σ, the normalized reflectance at normal incidence $R_{\text{norm}}(0°)$, and the corrected directionality coefficient Q_{Corr}. A value $Q_{\text{Corr}} \approx 1$ indicates near-Lambertian behavior, whereas $Q_{\text{Corr}} > 1$ corresponds to a more directional (super-Lambertian) profile and $Q_{\text{Corr}} < 1$ to a flatter, more diffuse (sub-Lambertian) profile.

Table 5. Angular reflectance statistics computed over the range $[-85°, 85°]$. $\Delta\bar{R}$ and ΔR_{max} are the mean and maximum deviations from the ideal cosine law; Σ quantifies bilateral asymmetry; $R_{\text{norm}}(0°)$ and Q_{Corr} describe the normalized peak reflectance and the global directionality. A Lambertian surface has $Q_{\text{Corr}} = 1$.

Sample	$\Delta\bar{R}$ (%)	ΔR_{max} (%)	Σ (%)	$R_{\text{norm}}(0°)$ (%)	Q_{Corr}
REF99	5.29	17.06	0.51	100.00	1.03
$BaSO_4$	6.32	19.40	0.49	100.00	1.05
TiO_2	16.00	42.15	1.57	100.00	1.14
ASP	12.65	64.14	4.12	100.00	1.09
ATW	18.88	64.93	3.10	99.13	1.15
OWP	5.61	26.52	0.81	100.00	1.04

The Spectralon® 99 % reference exhibited the lowest mean error (5.29 %) and excellent symmetry (0.51 %), confirming the reliability of the measurement. Its $Q_{\text{Corr}} = 1.03$ indicates a slightly super-Lambertian behavior, likely due to weak residual specular contributions near $\theta = 0°$. Among the coatings, $BaSO_4$ showed the closest agreement with $R_{\text{ideal}}(\theta)$, with a mean deviation of 6.32 % and $Q_{\text{Corr}} = 1.05$. Office white paper (OWP) also showed low mean error (5.61 %) and low directionality ($Q_{\text{Corr}} = 1.04$), though with higher maximum error due to its fibrous texture. TiO_2 exhibited stronger angular dependence (16.00 %) and higher directionality ($Q_{\text{Corr}} = 1.14$), indicating a partially specular component. Commercial paints (ATW, ASP) showed the largest deviations (65 % max error, approximately) and the highest Q_{Corr} values, reflecting strong super-Lambertian behavior. Overall, $BaSO_4$ provided the most Lambertian angular response among the tested coatings.

5. DISCUSSION

Visual inspection of the coated samples provided complementary evidence to the quantitative reflectance analysis, linking surface morphology and finish to the measured optical performance. Representative samples are shown in Figure 9, illustrating the different surface textures and visual appearances obtained with each coating.

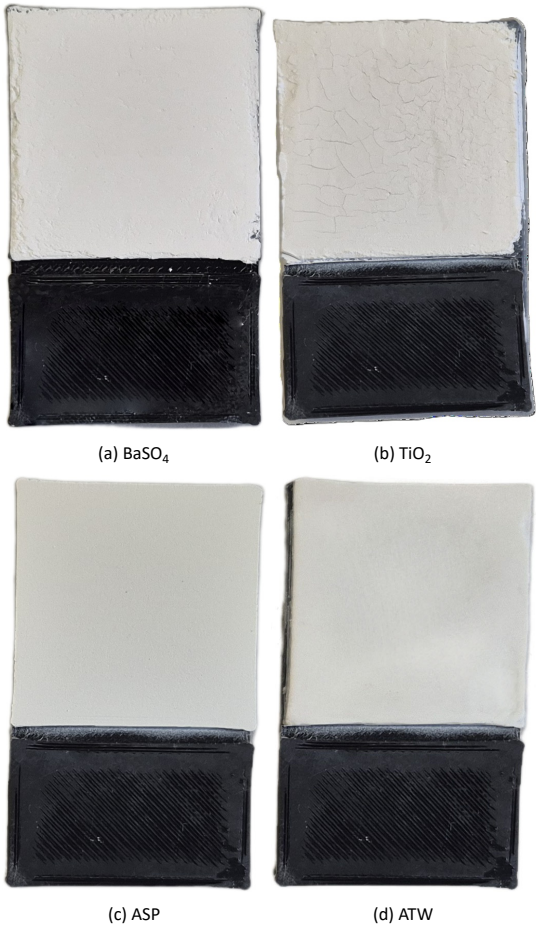

Figure 9. Photographs of representative coated samples used for reflectance characterization. $BaSO_4$ exhibits a uniform matte surface with good adhesion, while TiO_2 shows visible cracks and slight yellowing after drying. Acrylic and spray paints present glossier, less diffusive finishes compared to powder-based coatings.

The $BaSO_4$ coating produced a matte, homogeneous, and fully opaque surface with excellent adhesion on the PLA substrate. Its visual uniformity and diffuse appearance are consistent with the nearly ideal Lambertian behavior observed experimentally, with a mean hemispherical reflectance of 98.9 % and an angular deviation of only 6.3 % from the cosine law. No cracking or chromatic variation was observed after drying, confirming good mechanical stability and long-term reflectance uniformity.

The TiO_2 coating appeared smoother and glossier, with thin layers showing partial translucency and thicker deposits prone to cracking upon complete drying (Figure 9b). The surface also exhibited gradual yellowing over time, likely due to oxidation and rutile phase formation. These effects reduce diffuse scattering and explain the stronger angular dependence observed in Figure 8, where reflectance decreases markedly within the central angular region ($|\theta| < 20°$) and slightly recovers at higher viewing angles. Although its mean hemispherical reflectance remained high (96.6 %), the reduced Lambertian behavior, combined with moderate aging and mechanical fragility, makes TiO_2 less suitable for repeated or long-term laboratory measurements that require stable and uniform reflective behavior.

Commercial acrylic spray paint (ASP) and brush-applied acrylic titanium white paint (ATW) provided lower hemispherical reflectance values (79.7 % and 86.3 %, respectively) and higher angular deviations (12.7 % and 18.9 %). Their glossy and slightly uneven finishes introduced partial specular reflection and nonuniform scattering, particularly in the acrylic coating. Among the two, the spray paint was the easiest to apply uniformly and produced the most consistent surface coverage. Both coatings exhibited good mechanical resistance and stable reflectance across the visible range, though a gradual decrease was observed in the near-infrared region. Light sanding after drying improved uniformity but did not restore fully diffuse behavior. Overall, these materials offer practical and durable solutions for general-purpose optical setups, though their scattering performance remains below that of the Spectralon reference and $BaSO_4$ coating.

Office white paper (OWP) exhibited intermediate hemispherical reflectance (81.4 % on average, ranging from 76.2 % to 85.3 %) but excellent angular performance, with a mean deviation of only 5.6 % from the cosine law and high bilateral symmetry (0.8 %). Its surface provided highly diffuse scattering, comparable to the Spectralon® reference in terms of angular uniformity, although at lower absolute reflectance. However, its practical application in optical prototyping is severely restricted. Spectrally, the response is affected by paper texture and optical brighteners, causing non-uniformity. Mechanically, paper is limited to planar or simple developable surfaces and cannot be applied to small, complex, or doubly curved 3D-printed geometries (such as the parabolic reflector in Figure 10) without introducing seams or artifacts. Therefore, while OWP serves as a valid temporary reference for flat setups, it is unsuitable as a permanent coating for custom optical components.

In summary, these findings demonstrate that $BaSO_4$ provides the most stable, uniform, and Lambertian coating among the tested materials. TiO_2 offers a highly reflective but less diffuse alternative, while commercial paints and paper represent practical yet non-ideal options. The combined hemispherical and angular analyses confirm that surface uniformity and microstructure critically determine the optical diffusivity and suitability of reflective coatings for precise radiometric and optical systems.

The fabrication process used for the 30 mm × 30 mm planar samples, based on drop-casting of the $BaSO_4$ or TiO_2 suspensions with an intermediate acrylic binder layer, proved effective for obtaining uniform coatings but required patience and careful handling. A very light sanding step after drying was essential to homogenize the surface finish and remove minor irregularities.

For larger or curved substrates, an alternative deposition method based on airbrushing was also evaluated. This approach follows the same principle but provides superior control over coating thickness and uniformity. As an example, a 3D-printed PLA parabolic surface with a radius of curvature of 100 mm (Figure 10) was coated using the same $BaSO_4$ suspension (30 % w/w in distilled water) applied with a 0.3 mm nozzle airbrush at 2 bar pressure. Between each of the five applied layers, a thin film of transparent acrylic binder (see Section 3.1.) was sprayed to improve adhesion and minimize surface cracking. Maintaining the suspension well mixed throughout the process was crucial to prevent particle sedimentation and ensure optical uniformity. The resulting coating exhibited a smooth, highly diffusive matte finish, demonstrating the suitability of this multilayer airbrushing process for coating curved optical components.

Figure 10. Example of a 3D-printed PLA parabolic reflector (diameter 100 mm) coated with a $BaSO_4$-based suspension applied by airbrushing. The multilayer process with intermediate acrylic binder yielded a uniform, matte, and diffusively reflective surface.

6. CONCLUSIONS

The characterization of low-cost reflective coatings on 3D-printed PLA substrates identified $BaSO_4$ as the superior candidate for optical prototyping. The $BaSO_4$ coating demonstrated near-ideal performance, achieving an average hemispherical reflectance of 98.9 % and a Lambertian angular response with a mean deviation of only 6.3 % from the cosine law. In contrast, TiO_2 coatings, despite high reflectance (96.6 %), exhibited stronger spectral dependence and mechanical fragility. Commercial acrylic paints (ASP, ATW) proved unsuitable for metrological applications due to significant specular reflection and marked directionality ($Q_{\mathrm{Corr}} > 1.09$). The proposed multilayer deposition process—adaptable from drop-casting to airbrushing—proved cost-effective and compatible with complex additive-manufactured geometries, such as parabolic reflectors or custom integrating spheres. This approach effectively enables the fabrication of custom, broadband diffusers and calibration standards directly on 3D-printed optical components. Future work will focus on binder optimization to further enhance long-term mechanical durability and spectral stability in the UV range.

AUTHORS' CONTRIBUTION

G. Gibertoni: conceptualization, methodology, investigation, data curation, formal analysis, visualization, writing – original draft.
L. Rovati: supervision, validation, writing – review and editing.

REFERENCES

[1] P. W. Barber, R. C. Dunn, Diffuse Reflectance and Transmittance, Academic Press, 2014, vol. 46.
DOI: 10.1016/B978-0-12-386022-4.00006-6

[2] M. Janecek, Reflectivity Spectra for Commonly Used Reflectors, IEEE Transactions on Nuclear Science, vol. 59, Jun. 2012, no. 3, pp. 490–497.
DOI: 10.1109/TNS.2012.2183385

[3] R. Basri, D. Jacobs, Lambertian reflectance and linear subspaces, IEEE Transactions on Pattern Analysis and Machine Intelligence, vol. 25, Feb. 2003, no. 2, pp. 218–233.
DOI: 10.1109/TPAMI.2003.1177153

[4] R. S. Hunter, Description and Measurement of White Surfaces, JOSA, vol. 48, Sep. 1958, no. 9, pp. 597–605.
DOI: 10.1364/JOSA.48.000597

[5] E. R. Young, K. C. Clark, R. B. Bennett, T. L. Houk, Measurements and parameterization of the bidirectional reflectance factor of $BaSO_4$ paint, Applied Optics, vol. 19, Oct. 1980, no. 20, pp. 3500–3505.
DOI: 10.1364/AO.19.003500

[6] A. ul Rehman, I. Ahmad, S. A. Qureshi, Biomedical Applications of Integrating Sphere: A Review, Photodiagnosis and Photodynamic Therapy, vol. 31, Sep. 2020, p. 101712.
DOI: 10.1016/j.pdpdt.2020.101712

[7] J. B. Schutt, J. F. Arens, C. M. Shai, E. Stromberg, Highly Reflecting Stable White Paint for the Detection of Ultraviolet and Visible Radiations, Applied Optics, vol. 13, Oct. 1974, no. 10, pp. 2218–2221.
DOI: 10.1364/AO.13.002218

[8] S. D. Noble, A. Boeré, T. Kondratowicz, T. G. Crowe, R. B. Brown, D. A. Naylor, Characterization of a low-cost diffuse reflectance coating, Canadian Journal of Remote Sensing, vol. 34, Jan. 2008, no. 2, pp. 68–76.
DOI: 10.5589/m08-012

[9] Labsphere, Inc., Spectralon® White Diffuse Reflectance Standard (99%), Labsphere, Inc., North Sutton, NH, USA, 2021, product Specification. Online. [Accessed: 17 April 2026].
https://www.labsphere.com

[10] Avian Technologies LLC, Avian-B White Reflectance Coating, Avian Technologies LLC, New London, NH, USA, 2019, product Information Sheet. Online. [Accessed: 17 April 2026].
https://www.aviantechnologies.com

[11] Labsphere, Inc., 6080 White Diffuse Reflectance Coating, Labsphere, Inc., North Sutton, NH, USA, 2020, technical Data Sheet. Online. [Accessed: 17 April 2026].
https://www.labsphere.com

[12] Q. Gao, X. Wu, Z. Xia, Y. Fan, Coating mechanism and near-infrared reflectance property of hollow fly ash bead/TiO2 composite pigment, Powder Technology, vol. 305, Jan. 2017, pp. 433–439.
DOI: 10.1016/j.powtec.2016.10.037

[13] C. Dias, R. C. Veloso, J. Maia, N. M. M. Ramos, J. Ventura, Oversight of radiative properties of coatings pigmented with TiO2 nanoparticles, Energy and Buildings, vol. 271, Sep. 2022, p. 112296.
DOI: 10.1016/j.enbuild.2022.112296

[14] X. Li, J. Peoples, P. Yao, X. Ruan. Remarkable daytime sub-ambient radiative cooling in BaSO4 nanoparticle films and paints.
DOI: 10.48550/arXiv.2011.01161

[15] H. M. G. Teixeira, I. Serrano-Pedraza, D. H. Foster, Optical Stimulation Systems for Studying Human Vision, Elsevier, 2022, vol. 273, pp. 13–36.
DOI: 10.1016/bs.pbr.2022.04.003

[16] M. Gao, B. V. Nagy, Photometric simulation and uniformity optimization of a novel Ganzfeld-design, Optik, vol. 265, Sep. 2022, p. 169495.
DOI: 10.1016/j.ijleo.2022.169495

[17] M. Gao, B. V. Nagy, Simulation and experimental research on luminance uniformity in full-field electroretinogram stimulators, Optik, vol. 296, Feb. 2024, p. 171544.
DOI: 10.1016/j.ijleo.2023.171544

[18] G. Gibertoni, A. B. P. Irungovel, S. Viswanathan, L. Rovati, Silent stimulation of cones: A comparison between the ERG and PLR responses, Ophthalmic Technologies XXXIII, SPIE, Mar. 2023, vol. 12360, pp. 156–166.
DOI: 10.1117/12.2647380

[19] R. D. Gunkel, D. R. Bergsma, P. Gouras, A Ganzfeld Stimulator For Electroretinography, Archives of Ophthalmology, vol. 94, Apr. 1976, no. 4, pp. 669–670.
DOI: 10.1001/archopht.1976.03910030333017

[20] C. Zhang, N. C. Anzalone, R. P. Faria, J. M. Pearce, Open-Source 3D-Printable Optics Equipment, PLOS ONE, vol. 8, Mar. 2013, no. 3, p. e59840.
DOI: 10.1371/journal.pone.0059840

[21] M. Rank, A. Sigel, Y. Bauckhage, S. Suresh-Nair, M. Dohmen, C. Eder, C. Berge, A. Heinrich, 3D Printing of Optics Based on Conventional Printing Technologies, Springer International Publishing, Cham, 2021, pp. 45–167.
DOI: 10.1007/978-3-030-58960-8_3

[22] G. Berglund, A. Wisniowiecki, J. Gawedzinski, B. Applegate, T. S. Tkaczyk, Additive manufacturing for the development of optical/photonic systems and components, Optica, vol. 9, Jun. 2022, no. 6, pp. 623–638.
DOI: 10.1364/OPTICA.451642

[23] H. Gao, J. An, C. K. Chua, D. Bourell, C.-N. Kuo, D. T. H. Tan, 3D printed optics and photonics: Processes, materials and applications, Materials Today, vol. 69, Oct. 2023, pp. 107–132.
DOI: 10.1016/j.mattod.2023.06.019

[24] Y. Zhu, T. Tang, S. Zhao, D. Joralmon, Z. Poit, B. Ahire, S. Keshav, A. R. Raje, J. Blair, Z. Zhang, X. Li, Recent advancements and applications in 3D printing of functional optics, Additive Manufacturing, vol. 52, Apr. 2022, p. 102682.
DOI: 10.1016/j.addma.2022.102682

[25] G. Gibertoni, G. Borghi, L. Rovati, Compact High-Resolution Multi-Wavelength LED Light Source for Eye Stimulation, Electronics, vol. 13, Jan. 2024, no. 6, p. 1127.
DOI: 10.3390/electronics13061127

[26] G. Gibertoni, V. D. Pinto, S. Cattini, F. Tramarin, M. Geiser, L. Rovati, A simple Maxwellian optical system to investigate the photoreceptors contribution to pupillary light reflex, Ophthalmic Technologies XXXII, SPIE, Mar. 2022, vol. 11941, pp. 52–60.
DOI: 10.1117/12.2608129

[27] K. Willis, E. Brockmeyer, S. Hudson, I. Poupyrev, Printed optics: 3D printing of embedded optical elements for interactive devices, Proceedings of the 25th Annual ACM Symposium on User Interface Software and Technology, Association for Computing Machinery, New York, NY, USA, Oct. 2012, ser. UIST '12, pp. 589–598.
DOI: 10.1145/2380116.2380190

[28] V. Di Pinto, G. Gibertoni, L. Rovati, Investigation of a high-reflectance coating for wide-spectrum visual stimulation, 2025 IMEKO TC2 International Symposium on Modern Photonic Metrology, Modena, Italy, Sep. 2025.
DOI: 10.21014/tc2-2025.010

[29] G. Kortüm, W. Braun, G. Herzog, Principles and Techniques of Diffuse-Reflectance Spectroscopy, Angewandte Chemie International Edition in English, vol. 2, 1963, no. 7, pp. 333–341.
DOI: 10.1002/anie.196303331

[30] G. T. Georgiev, J. J. Butler, BRDF study of gray-scale Spectralon, Earth Observing Systems XIII, SPIE, Aug. 2008, vol. 7081, pp. 46–54.
DOI: 10.1117/12.795931

[31] Gigahertz-Optik, ODP97 Barium Sulfate Coating. Online. [Accessed: 17 April 2026].
https://www.gigahertz-optik.com/en-us/product/odp97/

[32] Titanium Dioxide for Architectural & Automotive Coatings: Ti-Pure™ R-706, The Chemours Company, Wilmington, DE, USA, 2025, ti-Pure™ R-706 rutile TiO_2 pigment for coatings. Online. [Accessed: 17 April 2026].
https://www.tipure.com/en/products/coatings/r-706

[33] European Aerosols, Technical Data Sheet – DUPLI-COLOR RAL Acryl Spray, Wolvega, Netherlands, 2025, product code 349805, RAL 9010 Pure White Matt. Gloss level 10 ± 2 GU at 60° (DIN 67530). Online. [Accessed: 17 April 2026].
https://duplicolor.eu/en/decorative/ral-acryl/ral-acryl

[34] Royal Talens, Safety Data Sheet – Amsterdam All Acrylics, Standard Series, Apeldoorn, The Netherlands, 2024, titanium White 105, water-based acrylic paint. Online. [Accessed: 17 April 2026].
https://www.amsterdam-acrylics.com/en/catalog/amsterdam-standard-series-acrylic/standard-series-acrylic-tube-120-ml-titanium-white-105/